

Nanoscale

Accepted Manuscript



This is an *Accepted Manuscript*, which has been through the Royal Society of Chemistry peer review process and has been accepted for publication.

Accepted Manuscripts are published online shortly after acceptance, before technical editing, formatting and proof reading. Using this free service, authors can make their results available to the community, in citable form, before we publish the edited article. We will replace this *Accepted Manuscript* with the edited and formatted *Advance Article* as soon as it is available.

You can find more information about *Accepted Manuscripts* in the [Information for Authors](#).

Please note that technical editing may introduce minor changes to the text and/or graphics, which may alter content. The journal's standard [Terms & Conditions](#) and the [Ethical guidelines](#) still apply. In no event shall the Royal Society of Chemistry be held responsible for any errors or omissions in this *Accepted Manuscript* or any consequences arising from the use of any information it contains.

Computational Design of Nanoparticle Drug Delivery Systems for Selective Targeting

Gregg A. Duncan and Michael A. Bevan*

Chemical & Biomolecular Engineering, Johns Hopkins University, Baltimore, MD 21218

Abstract

Ligand-functionalized nanoparticles capable of selectively binding to diseased versus healthy cell populations are attractive for improved efficacy of nanoparticle-based drug and gene therapies. However, nanoparticles functionalized with high affinity targeting ligands may lead to undesired off-target binding to healthy cells. In this work, Monte Carlo simulations were used to quantitatively determine net surface interactions, binding valency, and selectivity between targeted nanoparticles and cell surfaces. Dissociation constant, K_D , and target membrane protein density, ρ_R , are explored over a range representative of healthy and cancerous cell surfaces. Our findings show highly selective binding to diseased cell surfaces can be achieved with multiple, weaker affinity targeting ligands that can be further optimized by varying the targeting ligand density, ρ_L . Using the approach developed in this work, nanomedicines can be optimally designed for exclusively targeting diseased cells and tissues.

Introduction

Targeted nanoparticle drug delivery systems have gained much attention for the preferential delivery of medicine to diseased tissues with benefits including reduced damage to healthy tissues and significantly lowered dosages. In nanoparticle-based therapies, targeting agents can be introduced to the particle surface to allow for specific binding to membrane protein receptors with anomalous or over-abundant expression in diseased cells. If a membrane protein is exclusively expressed on diseased cells, functionalization with high affinity targets (*e.g.*, antibodies) allows for nanoparticles to bind strongly to cells with this protein present.^{1, 2} This strategy has been effective for a number of diseases such as arthritis,³ cancer,⁴ and multiple sclerosis.⁵ However, if the target protein is present at moderate levels on healthy cells, high-affinity targeting agents lose selectivity due to adherence to both diseased and healthy cells. In such situations, recent work has shown that binding selectivity can be recovered by engineering nanoparticles with weaker targeting affinity, which require multi-valent binding that can only be induced at cell surfaces with abnormally high expression of the target membrane protein. This has been demonstrated with targeting of integrins with the reactive tripeptide sequence of fibronectin, RGD,⁶⁻⁸ and targeting of CD44 with hyaluronic acid (HA)⁹⁻¹³ for cancer diagnostics and targeted therapies.

Designing nanoparticles for selective targeted delivery with experimental assays alone is challenging and labor intensive due to a variety of possible functionalization strategies. Comprehensive models of targeted nanoparticle therapies can provide guidance in choosing nanoparticle designs to narrow the parameter space for more efficient screening. Recent modeling efforts have aimed to characterize design parameters ranging from ligand binding affinity, ligand density, ligand tether length, tether valency (*i.e.*, bi-, tri-, tetravalent tethers),

* To whom correspondence should be addressed. email: mabevan@jhu.edu

nanoparticle shape, and substrate (cell surface) rigidity.¹⁴⁻²² Notably, Frenkel et. al.²³ developed an analytical model of ‘super-selective’ nanoparticle binding which demonstrated how weak, multi-valent binding allowed for selectivity for surfaces with high densities of target biomacromolecules. Binding affinities between ligands and target membrane proteins have been measured experimentally using fluorescence resonance energy transfer (FRET),²⁴ nuclear magnetic resonance (NMR),^{25, 26} and surface plasmon resonance (SPR).²⁷⁻²⁹ However, these indirect, ensemble measurements of ligand-protein association do not directly yield single and/or collective molecule binding energetics. In recent work, we have developed formalism to calculate K_D for an input ligand-receptor interaction potential allowing for realistic representations of these systems.³⁰ This same technique is applied in this study to represent specific target membrane proteins overexpressed on diseased cell surfaces. Few modeling efforts have considered using target membrane protein densities representative of both diseased and healthy cell populations. In order to design nanoparticles capable of selectively binding to diseased cells, it is crucial to also consider the degree of binding of nanoparticles onto healthy cells. Quantitative measurements of membrane protein expression have been made using flow cytometry for target membrane proteins on healthy and diseased cells³¹⁻³⁴ and we used these experimentally determined values as inputs into our model.

In this work, Monte Carlo (MC) computer simulations are used to measure the net interactions between ligand decorated nanoparticles and membrane proteins on healthy and diseased cell surfaces. Parameters most relevant towards the design of targeted drug delivery nanoparticles were explored to determine their effect on net surface interactions, binding valency, and selectivity for diseased cell surfaces. For example, K_D determines how strongly the ligand and protein interact which leads to changes in net interactions between nanoparticles and cell surfaces. Since weaker binding affinities are most relevant toward selective targeting strategies, K_D in the μM to mM range were explored. As a representative case, the membrane protein CD44, overexpressed in many cancerous cell types,³⁵⁻³⁹ was studied in this work as it has been exploited in cancer nanomedicines by surface functionalization with HA as a targeting ligand. In order to investigate realistic membrane protein densities for healthy and cancerous cells, a range of membrane protein densities were chosen based on flow cytometry measurements of CD44 expression on healthy platelets and colon carcinoma cells.⁴⁰ In modeling these highly complex biological systems, exploring parameters that closely match those in real systems will better demonstrate what is required to design nanoparticles with high selectivity for diseased cells and tissues. Using our approach, a design map is constructed that shows the optimal degree of functionalization with targeting ligands to achieve selective binding to cancerous versus healthy cells and tissues.

Methods

Ligand-Membrane Protein Interaction Potential

Membrane protein receptors with an effective radius, a_R , interact specifically with ligands on the particle surface represented as points in space. For the membrane receptor-ligand potential, U_{RL} , we use the form,

$$U_{RL}(r, a_R) = \begin{cases} \infty, & r \leq a_R \\ (1/2)k_s(r - a_R)^2 - |U_M|, & a_R < r < a_R + \delta \\ 0, & r \geq a_R + \delta \end{cases} \quad (1)$$

where r is the ligand-membrane protein separation, k_s is an effective spring constant, U_M is the receptor-ligand attractive well depth, and δ is the range of the attractive well as given by,

$$\delta = \left(2|U_M|/k_s\right)^{0.5} \quad (2)$$

The goal in this work is to model the specific interactions of biomacromolecules in these systems with well-defined association equilibria and using the formalism developed in prior work,³⁰ K_D is calculated for each input U_{RL} . Hard sphere interactions exist between the remaining components in the system.

Monte Carlo Simulations

As is illustrated in Figure 1, a 200 nm nanoparticle decorated with ligand receptors distributed with equal spacing on its surface was allowed to translate and rotate in 3D above a protein receptor functionalized substrate (*i.e.*, cell surface). Generation of ligand configurations and execution of nanoparticle rotations is described in detail in our prior work.³⁰ Target membrane proteins were represented as spheres with radius $a_R = 5$ nm that diffuse in 2D above the cell surface with a surface area of $1 \mu\text{m}^2$ and interact specifically with ligands on the particle surface as described above (Eq. 1). The radius of the membrane proteins in our study were estimated based on the size of the extracellular hyaluronic acid-binding domain of CD44 as determined by X-ray crystallography/NMR.⁴¹ Ligands are placed $(a_R + \delta)$ normal to the particle surface to prevent steric hindering of ligand-membrane protein binding. The particles are allowed to equilibrate above the surface for 5×10^5 MC steps and particle-cell surface separation, h , is then monitored for 2×10^7 MC steps. Histograms of h sampled, $p(h)$, are constructed and potentials of mean force, $W(h)$, are determined with a Boltzmann probability analysis as,

$$\left[W(h) - W(h_0)\right] / kT = -\ln\left[p(h) / p(h_0)\right] \quad (3)$$

where $W(h_0 = 100 \text{ nm}) = 0 kT$ was chosen as the reference state in each case as at this height, nanoparticles are outside of range for ligand-receptor mediated bridging interactions with the cell. The number of ligand-membrane protein bonds, N_B , was monitored in each step and histograms were constructed for each sampled binding valency. The fraction of bound particle configurations, where $N_B \geq 1$, was also monitored over the course of each simulation.

Results & Discussion

Particle-Cell Net Interaction Potentials

Nanoparticle-cell interaction potentials were determined for a range of membrane protein targets with varying levels of expression. By constructing histograms from the h sampled in each case, potential energy profiles can be determined using Eq. (3). In Fig. 2, particle-cell surface interaction potentials are shown for fixed particle ligand density, $\rho_L = 1820/\mu\text{m}^2$, and 5 different membrane protein surface receptor densities, ρ_R , over a physiologically relevant range ($64/\mu\text{m}^2 - 256/\mu\text{m}^2$).⁴⁰ Ligand-membrane protein mediated particle-cell surface interaction potentials are then determined at each ρ_R for K_D ranging from 40 – 5200 μM , representative of K_D range for

CD44-HA,²⁵ to determine how affinity for the target membrane protein impacts the effective interaction of the particle with the cell.

In Fig. 2A, net particle-cell interaction potentials are shown at $\rho_R = 256/\mu\text{m}^2$ with K_D from 120-5200 μM . At $K_D = 5200 \mu\text{M}$ and 630 μM (black and red circles), the particle has no net attractive interactions with the cell surface and at $h < 10\text{nm}$, the particle has a net repulsive interaction the cell surface. Repulsive interactions with the cell surface at $h < 10 \text{ nm}$ ($2a_R$) are due to repulsive interactions between the membrane protein receptors and nanoparticle surface. At these low binding affinities (U_M from 1-2 kT), the effective particle-cell surface attraction generated by bonds formed is insignificant in comparison to the net repulsion due to the presence of membrane proteins on the cell surface. When the affinity is increased to $K_D = 460 \mu\text{M}$ and 120 μM (green and yellow circles), net attractive particle-cell interactions are induced once the receptors come within range of interacting with the membrane proteins at $h < 20 \text{ nm}$. The attractive well depth increases as a function of binding affinity as ensembles of ligand-membrane protein bonds form between the particle and the surface.

The expression of membrane proteins was decreased to measure these same particle-cell surface interactions with levels expected on healthy cells. Net particle-cell interaction potentials were determined for $\rho_R = 196/\mu\text{m}^2$ (Fig. 2B), $100/\mu\text{m}^2$ (Fig. 2C), and $64/\mu\text{m}^2$ (Fig. 2D). It is again seen at lower binding affinity cases with $K_D = 5200 \mu\text{M}$ and 630 μM (black and red), no net attraction is generated as one would expect with lowered membrane protein densities. The net repulsion due to hard sphere interactions between the particle and surface ligands with the membrane proteins decreases in strength as their density on the cell surface decreases. As the affinity increases to $K_D = 460 \mu\text{M}$ and 120 μM , net attractive interactions are again induced with the magnitude of the attractive well depth decreasing as membrane protein density decreases. In Fig. 2B and C, potentials are not shown for $K_D = 40 \mu\text{M}$ ($U_M = 5 kT$) as the nanoparticle remained tightly bound the cell surface the duration of the simulation and interaction potential could not be calculated from equilibrium sampling using Eq. 3.

In Fig. 2C and D, potentials are shown for $K_D = 40 \mu\text{M}$ as adequate sampling was obtained for these lower membrane protein densities. However, the attractive well depth for this case only decreases to $\sim 3 kT$ at the lowest (healthy) cell expression levels shown which would lead to significant association of the particle to the cell. Irreversible binding to the cell surface independent of ρ_R was observed for all cases with $K_D < 40\mu\text{M}$. The irreversible binding seen in these cases is indicative of very strong net attraction ($W \ll -5 kT$) to both healthy (low ρ_R) and cancer (high ρ_R) cell surfaces. Due to the strong interactions in these cases, only small height fluctuations were observed over the course of the simulation and potential profiles could not be quantitatively determined for these cases. Alternative methods such as umbrella sampling can be used to determine potential profiles with strong net nanoparticle-cell surface interactions.³⁰ In the following sections, targeting ligands with higher binding affinity will also be characterized to determine their impact on binding valency and selectivity of binding to cell surfaces.

Particle-Cell Surface Binding Valency: Fixed ρ_L , Varying K_D

To introduce selectivity for specific cell surfaces, ligand-membrane protein mediated interaction potentials can be tailored based on K_D and ρ_R of the target membrane protein. Binding valency on the particle scale becomes an important factor in designing particles selective to diseased cells with specific membrane protein expression levels. For weaker affinity targets with K_D in μM range, multiple ligand-membrane protein bonds form in parallel to

generate significant net particle-cell attraction as shown in Fig. 2. Fig. 3 illustrates how this particle-cell binding valency varies over a range of K_D and ρ_R for nanoparticles with $\rho_L = 1820/\mu\text{m}^2$.

In Fig. 3A-C, representative snapshots are shown from below the particle to show the number of bonds present with $K_D = 120 \mu\text{M}$ and $N_L = 229$ at varied ρ_R . This glass-bottom view of the particle above the cell surface helps to visualize how particle-cell binding valency changes at each membrane surface density. For the membrane proteins (small spheres), a linear 8-bit color scale is used to indicate receptor-ligand binding energy, U_{RL} , where particles turn from white when unbound ($U_{RL} = 0$) to red when tightly bound ($U_{RL} = U_M$). When $\rho_R = 64/\mu\text{m}^2$ shown in Fig. 3A, only a single bond is present between the particle and cell surface. When $\rho_R = 144/\mu\text{m}^2$ shown in Fig. 3B, multi-valent particle-cell binding is seen with 3 ligand-protein bonds formed simultaneously. Particle-cell binding valency further increases at $\rho_R = 256/\mu\text{m}^2$, shown in Fig 3C, with 6 bonds present. The binding energy of each bond formed also varies in magnitude and is clearly shown in each case with the U_{RL} color scale in Fig. 4. The number of bonds and distribution of bond energies will ultimately determine the net interaction induced between the particle and surface.

In Figure 3D, the mode of the particle-cell binding valency from all bound particle configurations is shown as a function of K_D and ρ_R for more quantitative comparison. The mode of binding valency, $\text{mode}(N_B)$, is the number of bridges most frequently present between the nanoparticle and cell during the course of each simulation. This value represents the most likely binding configuration sampled by the nanoparticle on the cell surface and clearly shows how binding valency changes as a function of K_D , ρ_L , and ρ_R . For the weakest binding affinities with K_D from $5200 \mu\text{M}$ - $460 \mu\text{M}$, the particle-cell interactions are largely monovalent which explains the weak net particle-cell interactions seen in Fig. 2. At $K_D = 120 \mu\text{M}$, particle-cell binding valency transitions from monovalent binding at low membrane protein densities to multi-valent binding at higher membrane protein densities. This shift in binding valency explains the sensitivity of the net particle-cell interactions to ρ_R seen in Fig. 3. Multi-valent binding valency occurs at all $K_D > 120 \mu\text{M}$ on each cell surface independent of membrane protein density. With multi-valent particle-cell binding at both healthy and diseased membrane protein expression levels, net attractive interactions will be present at all cell surfaces leading to a loss in selectivity.

Particle-Cell Surface Binding Valency: Fixed K_D , Varying ρ_L

The valency of particle-cell binding can also be tuned by changing the density of ligands, ρ_R , functionalized on the nanoparticle. This design parameter allows us to engineer nanoparticles to selectively bind to cells given a specific K_D and ρ_R . We demonstrate this for a target membrane protein with a specific $K_D = 460 \mu\text{M}$ and ρ_R varied from $64/\mu\text{m}^2$ (healthy cells) to $256/\mu\text{m}^2$ (diseased cells) with nanoparticles functionalized with varying densities of targeting ligands, ρ_L . Fig. 4 shows simulations snapshots to visualize changes in valency for each ρ_L investigated and in Fig. 4A-C with quantitative comparison of all cases in Fig. 4D.

In Fig. 4A-C, representative snapshots are shown again below the particle with an 8-bit linear color scale of U_{RL} for all membrane proteins for an example case with $\rho_R = 256/\mu\text{m}^2$. With $\rho_L = 810/\mu\text{m}^2$ (Fig. 4A), only a single bond is present between the particle and cell surface. With ρ_L increased to $1820/\mu\text{m}^2$ (Fig. 4B), multi-valent bonding is seen with 2 ligand-membrane protein bonds present. When ρ_L is further increased to $7300/\mu\text{m}^2$ (Fig. 4C), 7 membrane proteins

have tightly bound to ligand receptors on the particle. These snapshots clearly visualize how changes in ligand density on the nanoparticle surface greatly impact binding valency.

In Fig. 4D, we quantitatively examine the effects of ρ_L on particle-cell binding valency with cell surfaces with varied ρ_R . With $\rho_L = 810/\mu\text{m}^2$ and $1820/\mu\text{m}^2$, the particle only binds monovalently with the cell surface at all target membrane protein densities. At $\rho_L = 7300/\mu\text{m}^2$, we begin to see multi-valent binding that increases as a function of ρ_R . As ligand-membrane protein binding is highly reversible at such high K_D , larger numbers of ligands on the nanoparticle surface must be present for multiple ligand-receptor bonds to be formed in parallel. These results illustrate how binding valency can be tuned with particle design. In order to enhance selectivity in these systems, a shift from monovalent to high order, multi-valent binding allows for tuning of particle-cell interactions from weak and reversible to strong and irreversible. In the next section, we will discuss how nanoparticle design impacts binding and selectivity in these systems and what is required for selective targeting.

Binding vs. Selectivity of Targeted Nanomedicines for Cancer vs. Healthy Cells

Typically in designing nanoparticles for targeted cancer therapies, a target membrane protein is identified that is expressed at abnormally high levels on cancer cells compared to healthy cells. Nanoparticles can then be functionalized with a ligand that interacts specifically with the target membrane protein to preferentially bind to cancer cells. To measure the strength of binding to cancer cell surfaces, the fraction of bound states, θ , is monitored over the course of each simulation which is defined as,

$$\theta = S_b / S \quad (4)$$

where S is the total number of states and S_b is the number of states where the nanoparticle is bound to 1 or more membrane protein receptors ($N_b \geq 1$). θ is inversely proportional to $W(h)$ as the fraction of bound states will increase as $W(h)$ decreases (*i.e.* net attraction increases). While $W(h)$ can only be determined quantitatively for certain cases with adequate equilibrium sampling, θ can be calculated for all cases and serves as an order parameter to show the degree of nanoparticle binding to the cell surface allowing for comparison across a range of design parameters. This allows us to identify repulsive ($\theta=0$), reversible ($\theta<1$) and irreversible ($\theta=1$) binding between nanoparticles and cell surfaces based on measured θ . Selectivity, χ , is then defined as,

$$\chi = \theta_C / \theta_H \quad (5)$$

where the subscripts refer to cancer (C) and healthy (H) cell surfaces where $\rho_R = 256/\mu\text{m}^2$ and $\rho_R = 64/\mu\text{m}^2$, respectively. Figure 5 presents two-dimensional (2D) contour maps of specificity and selectivity as a function of ρ_L from 1000-7000// μm^2 and K_D from 10-5000 μM . The data shown in Figure 5 summarizes results from a total of 220 simulations and 2D contour maps allow us to clearly visualize how changes in ρ_L and K_D impact binding and selectivity in these systems.

The fraction of bound states, θ , as a function of ρ_L and K_D are shown in Fig. 5A where white indicates no binding to the cell surface ($\theta=0$) and red indicates strong binding to the cell surface ($\theta=1$). Irreversible binding to cancer cell surfaces is seen for $K_D < 100\mu\text{M}$ for all values of ρ_L evaluated and the density of targeting ligands appears to have little effect on net nanoparticle-cell surface interactions (inset image, closed red circle). For targeting ligands with K_D between 100-500 μM , binding at the cell surface becomes more sensitive to changes in ρ_L . At

$\rho_L > 3000/\mu\text{m}^2$, high θ values are observed indicating irreversible binding with the cell surface, and then transitions to intermediate θ at lower $\rho_L < 3000/\mu\text{m}^2$, indicating reversible binding. At $K_D > 500 \mu\text{M}$, low θ values are measured indicating ρ_L within this range of densities is insufficient to induce any binding at the cell surface (inset image, closed white circle). These findings are consistent with earlier results to show that more attractive receptor-ligand interactions (decreasing U_{RL} , K_D) or multi-valent binding dependent on ρ_L , lead to strong adhesion of targeted nanomedicines to the surface of cancer cells.

Next, the selectivity for cancer versus healthy cell surfaces as a function of ρ_L and K_D are shown in Fig. 5B where white indicates low selectivity ($\chi=1$) and blue indicates high selectivity ($\chi=5$). At $K_D < 30 \mu\text{M}$, low χ values are observed for all values of ρ_L and shows changes in ρ_L do not impact selectivity for targeting with these stronger binding affinities. Selectivity becomes more sensitive to changes in ρ_L with K_D between 30-200 μM where decreases in ρ_L lead to improvements (*i.e.*, an increase in χ) in selectivity. At $K_D > 200 \mu\text{M}$, high values of χ are observed for all ρ_L and it again appears to have little impact on selectivity. Overall, these results are consistent with our previous findings. Net particle-cell interactions are less sensitive to changes in ρ_L and ρ_R with targeting ligands of higher binding affinity ($K_D < 30 \mu\text{M}$) where multiple ligand-receptor bonds in parallel are not required to induce strong adhesion. The requirement of multi-valency on the particle scale becomes clear in the intermediate range of K_D from 30 to 200 μM and results in increasing χ with decreases in ρ_L . We find at even lower binding affinities that selectivity is relatively high for all values of ρ_L which may seem counter-intuitive, but it is important to remember that selectivity is a comparison of binding to healthy (low ρ_R) and cancer (high ρ_R) cell surfaces. While weak, reversible binding at cancer cell surfaces is observed for all ρ_L at these low binding affinities (Fig. 3A), binding can be further reduced at healthy cell surfaces with lower membrane protein density.

Optimal Design of Selective Targeted Nanomedicines

The ideal targeted cancer nanotherapy preferentially accumulates at the tumor site which requires nanoparticles to be adhesive to cancer cells and non-adhesive to healthy cells. The ultimate goal of our study is to design selective targeted nanomedicines with both of these qualities as we have discussed above, strong binding (high θ) and highly selective (high χ) to cancer cells. To determine optimal targeted nanomedicine designs with both of these properties, we introduce an empirically-derived selective targeting parameter, β , defined as,

$$\beta = \left[\frac{\theta - \min(\theta)}{\min(\theta) - \max(\theta)} \right] - \left[\frac{\chi - \min(\chi)}{\min(\chi) - \max(\chi)} \right] \quad (6)$$

where θ and χ are normalized to scale from 0 to 1 based on minimum and maximum measured values and thus equally contribute to β . The aim of β is to provide a single parameter that accounts for both the binding and selectivity of nanoparticle designs, as both of these qualities are important to selective targeting. For example, high affinity and significant binding to all cells, captured by increases in θ , while important for particle immobilization on cell surfaces does not favor selectivity. Multi-valent, weak specific interactions favor high selectivity, captured by a large χ . However, this effect works in opposition to significant particle binding onto cancer cell surfaces necessary for uptake. As a linear combination of θ and χ , β captures the trade-off between these two effects where it suggests an optimal when the two effects balance

each other. To illustrate the meaning of β with a few limiting cases, $\beta=-1$ indicates high selectivity and weak binding to cancer cells, $\beta=1$ indicates low selectivity and strong binding, and $\beta=0$ indicates a balance in binding and selectivity, optimal for targeting cancer cells. A 2D contour map of β as a function of ρ_L and K_D is shown in Fig. 6 with a linear spectrum color scale from blue when $\beta=-1$ to white when $\beta=0$, to red when $\beta=1$. With this color scheme, we are able to clearly distinguish the targeting characteristics of each design.

With this tri-color scale in Fig. 6, three distinct regimes become apparent in β as a function of K_D . In the red region of the map ($\beta>0$) at higher binding affinities, strong binding is induced at both healthy and cancer cell surfaces at all ρ_L explored in this work which leads to low selectivity. Designs in this red region will lead to off-target binding of healthy cell surfaces. In the white region of the map ($\beta\approx 0$) at intermediate binding affinities, nanoparticles show selective targeting of cancer cells that can be optimized as a function of ρ_L . In the blue region of the map ($\beta<0$) at low binding affinities, all cases show high selectivity, but will bind too weakly to cancer cell surfaces to accumulate at the tumor site. The trend is graphically shown with Fig. 6B-D where strong multi-valent binding is exhibited at both healthy and cancer cell surfaces in Fig. 6B (red region), multi-valent binding is exhibited at cancerous but not healthy cell surfaces in Fig. 6C (white region), and no binding is exhibited to either healthy or cancer cell surfaces in Fig. 6D (blue region).

These findings help to illustrate a few important design considerations for selective targeted nanomedicines. Ligands with weak affinity for target membrane proteins are best suited for use in selective targeting. Weak affinity targeting ligands with K_D on the order of μM require multi-valency on the particle scale to induce strong adhesive interactions at cell surfaces. Binding valency at diseased versus healthy surfaces can then be directly tuned by functionalizing nanoparticles with an optimal density of targeting ligands. Use of these computational screening methods for selective targeting can aid design of these systems. Future studies will consider the effects of additional design considerations including targeting ligand representation (*e.g.* polymer tethers), ligand valency, and nanoparticle shape to develop more comprehensive models of targeted nanoparticle drug delivery systems. We also aim in future work to develop analytical expressions to establish relationships between design parameters such as K_D , ρ_L , and ρ_R and simulation/experimental outcomes such as W , θ , χ , and β which will further enhance the interpretive and predictive capabilities of this model.

Conclusion

Interactions of targeted drug delivery nanoparticles with cell surfaces representative of cancerous and healthy tissues are investigated using Monte Carlo Simulations with realistic, experimentally verified binding affinities and membrane protein expression levels. By measuring interactions of nanoparticles with both cancer cells having abnormal over-expression of target proteins and healthy cells expressing normal levels of target proteins, our results show that multi-valent nanoparticle-cell binding mediated by weak, reversible ligand-membrane protein interactions proved the most effective means to engineer nanomedicines with selective binding to cancer cell surfaces. While higher binding affinity targets are attractive due to their specificity for target membrane proteins, they are most appropriate when only sparse amounts are present on healthy cells which is not always the case for many diseases. Using lower affinity ligands to target for cancer cells with marked overexpression of target membrane proteins, nanoparticles can be designed with the requirement of multi-valency on the nanoparticle scale to induce

adhesion to the cell surface leading to much improved selectivity for specific cell populations. With this model, design of selective targeting for drug delivery nanoparticles can be optimized for specific diseases and designs maps can be generated to identify the optimal density of targeting ligands. In future studies, comparisons between the net interactions determined using this computational model and experimental measurements of nanoparticle-cell interactions will verify the utility of this model and help to identify additional parameters for further refinement of our modeling approach.

Supplementary Information

Movie showing simulation renderings of targeted ($\rho_L=1820/\mu\text{m}^2$, $K_D=120 \mu\text{M}$) nanoparticle selective binding to cancer ($\rho_R = 256/\mu\text{m}^2$) vs. healthy ($\rho_R = 64/\mu\text{m}^2$) cell surfaces. Target membrane proteins have linear color scale depending on binding energy ranging from white when unbound ($U_{RL} = 0$) to red when tightly bound ($U_{RL} = U_M$).

Acknowledgments

We acknowledge support by the National Science Foundation through the following grants: CBET (0834125, 1066254) and IGERT (059430). We thank Dr. Brian Weitzner for assistance estimating size of HA-binding site of CD44 from crystallography data.

References

1. L. Brannon-Peppas and J. O. Blanchette, *Advanced Drug Delivery Reviews*, 2012, **64**, 206-212.
2. D. Schrama, R. a. Reisfeld and J. C. Becker, *Nature reviews. Drug discovery*, 2006, **5**, 147-159.
3. N. J. Olsen and C. M. Stein, *The New England journal of medicine*, 2004, **350**, 2167-2179.
4. E. L. Sievers and P. D. Senter, *Annual review of medicine*, 2013, **64**, 15-29.
5. J. W. Rose, J. Foley and N. Carlson, *Current neurology and neuroscience reports*, 2008, **8**, 419-426.
6. D. Arosio, L. Manzoni, E. M. V. Araldi and C. Scolastico, *Bioconjugate chemistry*, 2011, **22**, 664-672.
7. S. Kunjachan, R. Pola, F. Gremse, B. Theek, J. Ehling, D. Moeckel, B. Hermanns-Sachweh, M. Pechar, K. Ulbrich, W. E. Hennink, G. Storm, W. Lederle, F. Kiessling and T. Lammers, *Nano letters*, 2014.
8. A. J. Simnick, C. A. Valencia, R. Liu and A. Chilkoti, *ACS nano*, 2010, **4**, 2217-2227.
9. S. H. Bhang, N. Won, T.-J. Lee, H. Jin, J. Nam, J. Park, H. Chung, H.-S. Park, Y.-E. Sung, S. K. Hahn, B.-S. Kim and S. Kim, *ACS nano*, 2009, **3**, 1389-1398.
10. H.-J. Cho, H. Y. Yoon, H. Koo, S.-H. Ko, J.-S. Shim, J.-H. Lee, K. Kim, I. C. Kwon and D.-D. Kim, *Biomaterials*, 2011, **32**, 7181-7190.
11. K. Y. Choi, H. Chung, K. H. Min, H. Y. Yoon, K. Kim, J. H. Park, I. C. Kwon and S. Y. Jeong, *Biomaterials*, 2010, **31**, 106-114.
12. K. Y. Choi, H. Y. Yoon, J.-H. Kim, S. M. Bae, R.-W. Park, Y. M. Kang, I.-S. Kim, I. C. Kwon, K. Choi, S. Y. Jeong, K. Kim and J. H. Park, *ACS nano*, 2011, **5**, 8591-8599.
13. V. M. Platt and F. C. Szoka, *Molecular pharmaceuticals*, 2009, **5**, 474-486.
14. N. W. Moore and T. L. Kuhl, *Biophysical journal*, 2006, **91**, 1675-1687.
15. M. C. Hagy, S. Wang and E. E. Dormidontova, *Langmuir*, 2008, **24**, 13037-13047.

16. C.-z. Zhang and Z.-g. Wang, *Langmuir* 2007, **23**, 13024-13039.
17. S. Wang and E. E. Dormidontova, *Biomacromolecules*, 2010, **11**, 1785-1795.
18. A. S. Sarvestani, *Soft Matter*, 2013, **9**, 5927.
19. J. Liu, G. E. R. Weller, B. Zern, P. S. Ayyaswamy, D. M. Eckmann, V. R. Muzykantov and R. Radhakrishnan, *Proceedings of the National Academy of Sciences of the United States of America*, 2010, **107**, 16530-16535.
20. R. Vácha, F. J. Martinez-Veracoechea and D. Frenkel, *Nano letters*, 2011, **11**, 5391-5395.
21. R. Vácha, F. J. Martinez-Veracoechea and D. Frenkel, *ACS nano*, 2012, **6**, 10598-10605.
22. J. B. Haun and D. A. Hammer, *Langmuir*, 2008, **24**, 8821-8832.
23. F. J. Martinez-Veracoechea and D. Frenkel, *Proceedings of the National Academy of Sciences of the United States of America*, 2011, **108**, 10963-10968.
24. M. Parsons, A. J. Messent, J. D. Humphries, N. O. Deakin and M. J. Humphries, *Journal of cell science*, 2008, **121**, 265-271.
25. S. Banerji, A. J. Wright, M. Noble, D. J. Mahoney, I. D. Campbell, A. J. Day and D. G. Jackson, *Nature structural & molecular biology*, 2007, **14**, 234-239.
26. R. Meinecke and B. Meyer, *Journal of Medicinal Chemistry*, 2001, **44**, 3059-3065.
27. P. A. van der Merwe and A. N. Barclay, *Current Opinion in Immunology*, 1996, **8**, 257-261.
28. L.-k. Liu and B. C. Finzel, *Journal of medicinal chemistry*, 2014, **57**, 2714-2725.
29. M. K. Wild, M. C. Huang, U. Schulze-Horsel, P. a. van der Merwe and D. Vestweber, *The Journal of biological chemistry*, 2001, **276**, 31602-31612.
30. G. A. Duncan and M. A. Bevan, *Soft Matter*, 2014, **10**, 8524-8532.
31. L. Vellon, J. a. Menendez and R. Lupu, *Oncogene*, 2005, **24**, 3759-3773.
32. S. Pyne, X. Hu, K. Wang, E. Rossin, T.-I. Lin, L. M. Maier, C. Baecher-Allan, G. J. McLachlan, P. Tamayo, D. a. Hafler, P. L. De Jager and J. P. Mesirov, *Proceedings of the National Academy of Sciences of the United States of America*, 2009, **106**, 8519-8524.
33. D. B. Agus, J. F. Alexander, W. Arap, S. Ashili, J. E. Aslan, R. H. Austin, V. Backman, K. J. Bethel, R. Bonneau, W.-C. Chen, C. Chen-Tanyolac, N. C. Choi, S. A. Curley, M. Dallas, D. Damania, P. C. W. Davies, P. Decuzzi, L. Dickinson, L. Estevez-Salmeron, V. Estrella, M. Ferrari, C. Fischbach, J. Foo, S. I. Fraley, C. Frantz, A. Fuhrmann, P. Gascard, R. A. Gatenby, Y. Geng, S. Gerecht, R. J. Gillies, B. Godin, W. M. Grady, A. Greenfield, C. Hemphill, B. L. Hempstead, A. Hielscher, W. D. Hillis, E. C. Holland, A. Ibrahim-Hashim, T. Jacks, R. H. Johnson, A. Joo, J. E. Katz, L. Kelbaskas, C. Kesselman, M. R. King, K. Konstantopoulos, C. M. Kraning-Rush, P. Kuhn, K. Kung, B. Kwee, J. N. Lakin, G. Lambert, D. Liao, J. D. Licht, J. T. Liphardt, L. Liu, M. C. Lloyd, A. Lyubimova, P. Mallick, J. Marko, O. J. T. McCarty, D. R. Meldrum, F. Michor, S. M. Mumenthaler, V. Nandakumar, T. V. O'Halloran, S. Oh, R. Pasqualini, M. J. Paszek, K. G. Philips, C. S. Poultney, K. Rana, C. A. Reinhart-King, R. Ros, G. L. Semenza, P. Senechal, M. L. Shuler, S. Srinivasan, J. R. Staunton, Y. Stypula, H. Subramanian, T. D. Tlsty, G. W. Tormoen, Y. Tseng, A. van Oudenaarden, S. S. Verbridge, J. C. Wan, V. M. Weaver, J. Widom, C. Will, D. Wirtz, J. Wojtkowiak and P.-H. Wu, *Scientific reports*, 2013, **3**, 1449.
34. J. M. Irish, N. Kotecha and G. P. Nolan, *Nature reviews. Cancer*, 2006, **6**, 146-155.
35. T. Hiraga, S. Ito and H. Nakamura, *Cancer Research*, 2013, **73**, 4112-4122.
36. J. M. V. Louderbough and J. A. Schroeder, in *Molecular Cancer Research*, 2011, vol. 9, pp. 1573-1586.

37. D. Naor, S. Nedvetzki, I. Golan, L. Melnik and Y. Faitelson, *Critical reviews in clinical laboratory sciences*, 2002, **39**, 527-579.
38. L. Patrawala, T. Calhoun, R. Schneider-Broussard, H. Li, B. Bhatia, S. Tang, J. G. Reilly, D. Chandra, J. Zhou, K. Claypool, L. Coghlan and D. G. Tang, *Oncogene*, 2006, **25**, 1696-1708.
39. M. Zöller, *Nature reviews. Cancer*, 2011, **11**, 254-267.
40. C. S. Alves, M. M. Burdick, S. N. Thomas, P. Pawar and K. Konstantopoulos, *American journal of physiology. Cell physiology*, 2008, **294**, C907-916.
41. P. Teriete, S. Banerji, M. Noble, C. D. Blundell, A. J. Wright, A. R. Pickford, E. Lowe, D. J. Mahoney, M. I. Tammi, J. D. Kahmann, I. D. Campbell, A. J. Day and D. G. Jackson, *Molecular Cell*, 2004, **13**, 483-496.

Figure Captions

Figure 1. Schematic of receptor-ligand mediated nanoparticle-cell interactions.

Figure 2. Particle-cell surface interaction potentials for nanoparticles with targeting ligand density, $\rho_L = 1820/\mu\text{m}^2$ and membrane protein density, $\rho_R = 256/\mu\text{m}^2$ (A), $196/\mu\text{m}^2$ (B), $100/\mu\text{m}^2$ (C), and $64/\mu\text{m}^2$ (D) and receptor-ligand dissociation constant, $K_D = 5200 \mu\text{M}$ (black), $630 \mu\text{M}$ (red), $460 \mu\text{M}$ (green), and $120 \mu\text{M}$ (yellow) and $40 \mu\text{M}$ (blue).

Figure 3. Representative snapshots with glass-bottom view beneath nanoparticle with targeting ligand density, $\rho_L = 1820/\mu\text{m}^2$ and membrane protein density, $\rho_R = 64/\mu\text{m}^2$ (A), $144/\mu\text{m}^2$ (B), and $256/\mu\text{m}^2$ (C) and receptor-ligand dissociation constant, $K_D = 120 \mu\text{M}$. Target membrane proteins have linear color scale depending on binding energy, U_{RL} , ranging from white when unbound ($U_{RL} = 0$) to red when tightly bound ($U_{RL} = U_M$). (D) Mode binding valency, $\text{mode}(N_B)$, of surface-bound nanoparticle configurations as a function of K_D and ρ_R .

Figure 4. Representative snapshots with glass-bottom view beneath nanoparticle with targeting ligand density, $\rho_L = 810/\mu\text{m}^2$ (A), $1820/\mu\text{m}^2$ (B), and $7300/\mu\text{m}^2$ (C) and membrane protein density, $\rho_R = 256/\mu\text{m}^2$ and receptor-ligand dissociation constant, $K_D = 460 \mu\text{M}$. Target membrane proteins have linear color scale depending on binding energy, U_{RL} , ranging from white when unbound ($U_{RL} = 0$) to red when tightly bound ($U_{RL} = U_M$). (D) Mode binding valency, $\text{mode}(N_B)$, of surface-bound nanoparticle configurations as a function of K_D and ρ_L .

Figure 5. Two-dimensional (2D) contour maps of (A) binding to cancer cell surfaces and (B) selectivity for cancer versus healthy cell surfaces as a function of targeting ligand density, ρ_L , and receptor-ligand dissociation constant, K_D . Binding fraction, $\theta = \theta_C$, is shown on a linear spectrum color scale from white when $\theta = 0.01$ to red when $\theta = 1$ and selectivity, $\chi = \theta_C/\theta_H$, is shown on a linear color spectrum scale from white when $\chi = 1$ to blue when $\chi = 5$. The subscripts refer to cancer cell surface, C, where membrane protein density, ρ_R , is equal to $256/\mu\text{m}^2$ and healthy cell surface, H, where $\rho_R = 64/\mu\text{m}^2$. Inset images in (A) are representative snapshots with glass-bottom view beneath nanoparticle. Representative snapshots from healthy and cancer cell simulations are shown in (C) and (D) corresponding to the conditions marked with closed white and blue circles shown in (B).

Figure 6. Two-dimensional (2D) contour map of targeting selectivity for cancer versus healthy cell surfaces of targeting ligand density, ρ_L , and receptor-ligand dissociation constant, K_D . Selective targeting parameter, β (defined in Eq. 6), is shown on a linear spectrum color scale

from blue when $\beta=-1$ to white when $\beta=0$ to red when $\beta=1$. Based on this color scheme, blue indicates weak binding and high selectivity, red indicates strong binding and low selectivity, and white indicates a balance between binding and selectivity (*i.e.*, optimal for selective targeting). Representative snapshots from healthy and cancer cell simulations with a glass-bottom view beneath nanoparticles are shown in (B), (C) and (D) corresponding to the conditions marked with closed red, white and blue circles shown in (A).

Figure 1

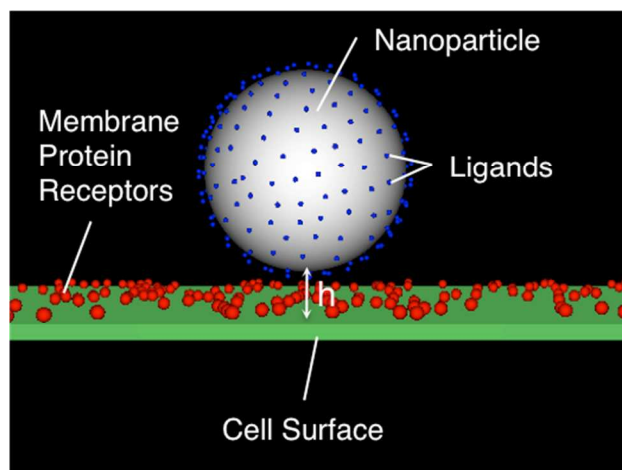


Figure 2

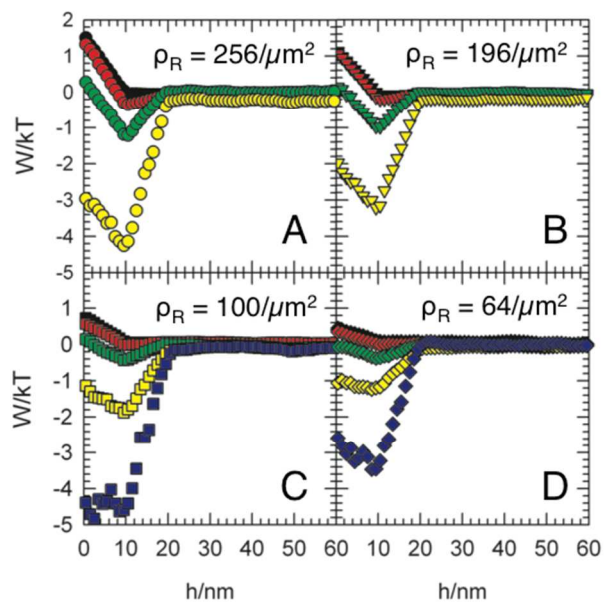


Figure 3

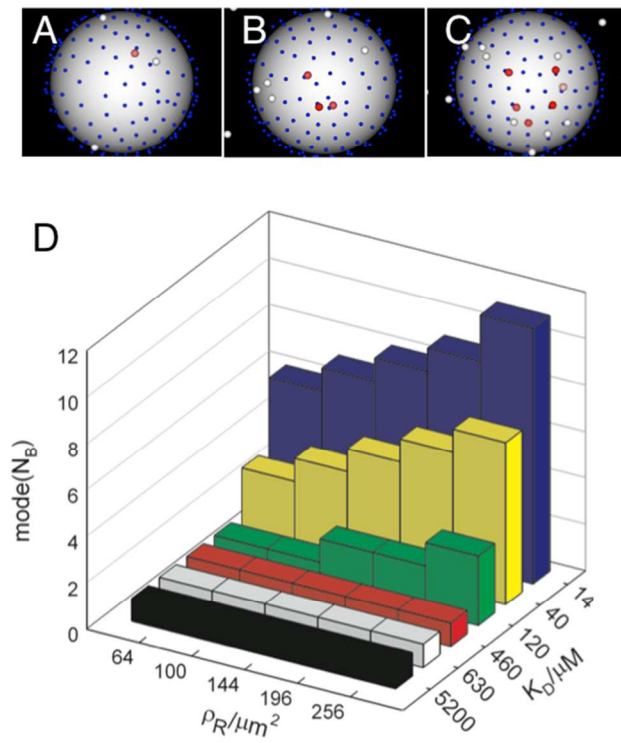


Figure 4

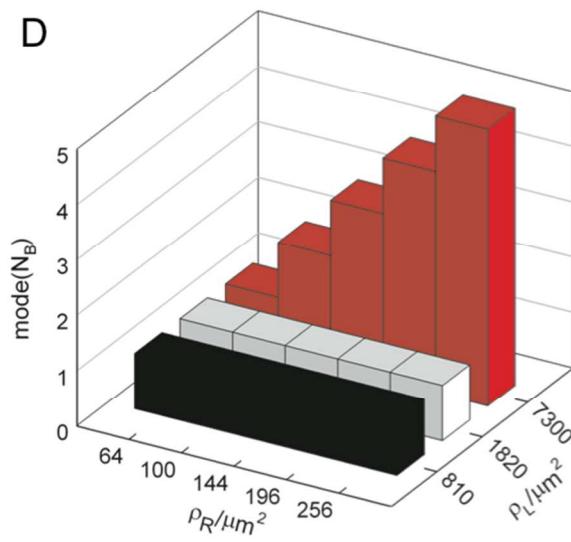
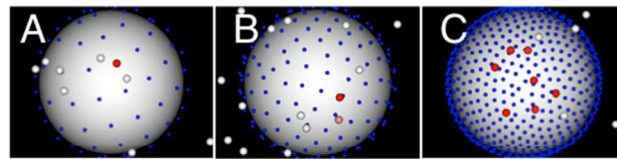


Figure 5

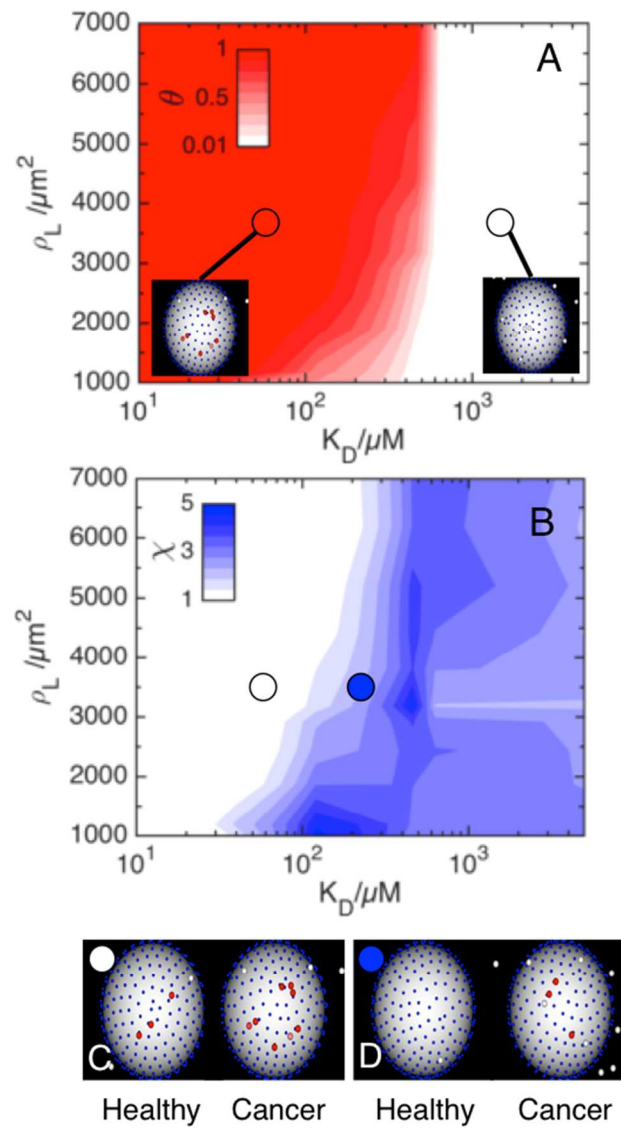
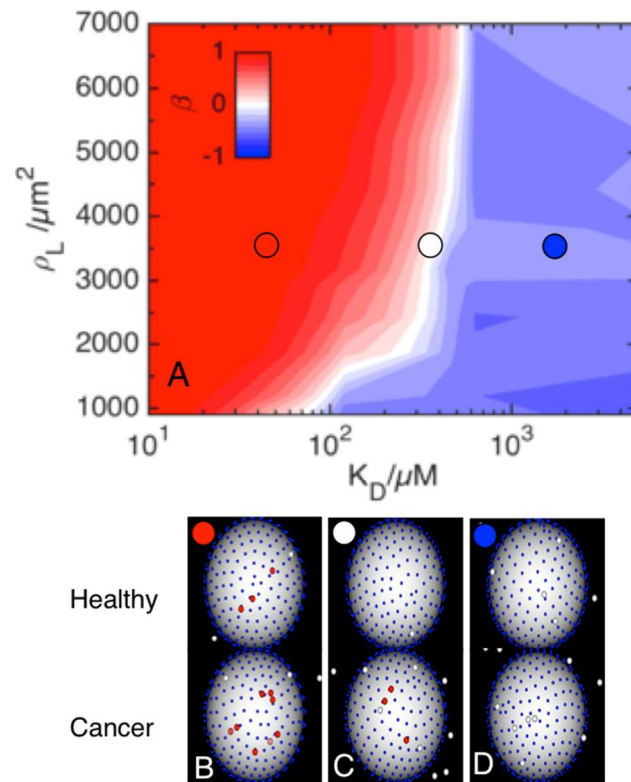
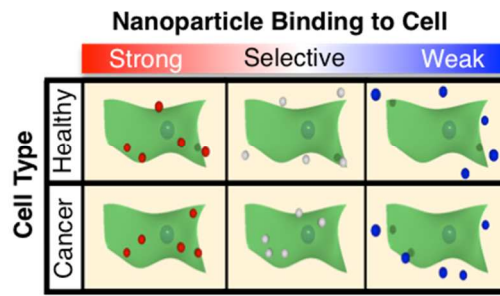


Figure 6



For Table of Contents Use Only (4 cm x 8 cm)
Computational Design of Nanoparticle Drug Delivery Systems for Selective Targeting
Gregg A. Duncan and Michael A. Bevan



Binding of targeted drug delivery nanoparticles to healthy and cancerous cells is investigated using Monte Carlo Simulations to determine the optimal degree of functionalization with ligands for selective targeting.